










Schwarzschild and Ledoux are Equivalent on Evolutionary Timescales

Evan H. Anders^{1,2} , Adam S. Jermyn^{2,3} , Daniel Lecoanet^{1,2,4} , Adrian E. Fraser^{2,5} , Imogen G. Cresswell^{2,6} ,
Meridith Joyce^{2,7} , and J. R. Fuentes⁸ 

¹CIERA, Northwestern University, Evanston IL 60201, USA; evan.anders@northwestern.edu

²Kavli Institute for Theoretical Physics, University of California, Santa Barbara, CA 93106, USA

³Center for Computational Astrophysics, Flatiron Institute, New York, NY 10010, USA

⁴Department of Engineering Sciences and Applied Mathematics, Northwestern University, Evanston IL 60208, USA

⁵Department of Applied Mathematics, Baskin School of Engineering, University of California, Santa Cruz, CA 95064, USA

⁶Department Astrophysical and Planetary Sciences & LASP, University of Colorado, Boulder, CO 80309, USA

⁷Space Telescope Science Institute, 3700 San Martin Drive, Baltimore, MD 21218, USA

⁸Department of Physics and McGill Space Institute, McGill University, 3600 rue University, Montreal, QC H3A 2T8, Canada

Received 2022 February 25; revised 2022 March 10; accepted 2022 March 10; published 2022 March 25

Abstract

Stellar evolution models calculate convective boundaries using either the Schwarzschild or Ledoux criterion, but confusion remains regarding which criterion to use. Here we present a 3D hydrodynamical simulation of a convection zone and adjacent radiative zone, including both thermal and compositional buoyancy forces. As expected, regions that are unstable according to the Ledoux criterion are convective. Initially, the radiative zone adjacent to the convection zone is Schwarzschild unstable but Ledoux stable due to a composition gradient. Over many convective overturn timescales, the convection zone grows via entrainment. The convection zone saturates at the size originally predicted by the Schwarzschild criterion, although in this final state the Schwarzschild and Ledoux criteria agree. Therefore, the Schwarzschild criterion should be used to determine the size of stellar convection zones, except possibly during short-lived evolutionary stages in which entrainment persists.

Unified Astronomy Thesaurus concepts: [Stellar convective zones \(301\)](#); [Stellar physics \(1621\)](#); [Stellar evolutionary models \(2046\)](#)

Supporting material: animation

1. Introduction

The treatment of convective boundaries in stars is a long-standing problem in modern astrophysics. Models and observations disagree about the sizes of convective cores (Claret & Torres 2018; Joyce & Chaboyer 2018; Viani & Basu 2020; Johnston 2021; Pedersen et al. 2021), the depths of convective envelopes (inferred from lithium abundances; Pinsonneault 1997; Sestito & Randich 2005; Carlos et al. 2019; Dumont et al. 2021), and the sound speed at the base of the Sun’s convection zone (see Basu 2016, Section 7.2.1). Inaccurate convective boundary specification can have astrophysical impacts by, e.g., affecting mass predictions of stellar remnants (Farmer et al. 2019; Mehta et al. 2022) and the inferred radii of exoplanets (Basu et al. 2012; Morrell 2020).

In order to resolve the many uncertainties involved in treating convective boundaries, it is first crucial to determine the boundary location. Some stellar evolution models determine the location of the convection zone boundary using the Schwarzschild criterion by comparing the radiative and adiabatic temperature gradients. In other models, the convection zone boundary is determined by using the Ledoux criterion, which also accounts for compositional stratification (Salaris & Cassisi 2017, Ch. 3, reviews these criteria). Recent work states that these criteria should agree on the location of the convective boundary (Gabriel et al. 2014; Paxton et al. 2018, 2019), but in practice, they can disagree (see Kaiser et al. 2020, Ch. 2), which

can affect asteroseismic observations (Silva Aguirre et al. 2011). Efforts to properly choose convective boundary locations have produced a variety of algorithms in stellar evolution software instruments (Paxton et al. 2018, 2019).

Multidimensional simulations can provide insight into the treatment of convective boundaries. Such simulations show that a convection zone adjacent to a Ledoux-stable region can expand by entraining material from the stable region (Meakin & Arnett 2007; Woodward et al. 2015; Jones et al. 2017; Cristini et al. 2019; Andrassy et al. 2020; Fuentes & Cumming 2020; Andrassy et al. 2021). However, past simulations have not achieved a statistically stationary state, leading to uncertainty in how to include entrainment in 1D models (Staritsin 2013; Scott et al. 2021).

In this Letter, we present a 3D hydrodynamical simulation with a convection zone that is adjacent to a Ledoux-stable but Schwarzschild-unstable region. Convection entrains material until the adjacent region is stable by both criteria. Our simulation demonstrates that the Ledoux criterion instantaneously describes the size of a convection zone. However, when the Ledoux and Schwarzschild criteria disagree, the Schwarzschild criterion correctly predicts the size at which a convection zone saturates. Therefore, when evolutionary timescales are much larger than the convective overturn timescale (e.g., on the main sequence; Georgy et al. 2021), the Schwarzschild criterion properly predicts convective boundary locations. When correctly implemented, the Ledoux criterion should return the same result (Gabriel et al. 2014). We discuss these criteria in Section 2, describe our simulation in Section 3, and briefly discuss the implications of our results for 1D stellar evolution models in Section 4.



Original content from this work may be used under the terms of the [Creative Commons Attribution 4.0 licence](#). Any further distribution of this work must maintain attribution to the author(s) and the title of the work, journal citation and DOI.

2. Theory and Experiment

The Schwarzschild criterion for convective stability is

$$\mathcal{Y}_S \equiv \nabla_{\text{rad}} - \nabla_{\text{ad}} < 0, \quad (1)$$

whereas the Ledoux criterion for convective stability is

$$\mathcal{Y}_L \equiv \mathcal{Y}_S + \frac{\chi_\mu}{\chi_T} \nabla_\mu < 0. \quad (2)$$

The temperature gradient $\nabla \equiv d \ln P / d \ln T$ (pressure P and temperature T) is ∇_{ad} for an adiabatic stratification and ∇_{rad} if all the flux is carried radiatively. The Ledoux criterion includes the effects of the composition gradient $\nabla_\mu = d \ln \mu / d \ln P$ (mean molecular weight μ), where $\chi_T = (d \ln P / d \ln T)_{\rho, \mu}$ and $\chi_\mu = (d \ln P / d \ln \mu)_{\rho, T}$ (density ρ).

Stellar structure software instruments assume that convective boundaries coincide with sign changes of \mathcal{Y}_L or \mathcal{Y}_S (Paxton et al. 2018, Section 2). The various stability regimes that can occur in stars are described in Section 3 and Figure 3 of Salaris & Cassisi (2017), but we note four important regimes here:

1. *Convection zones (CZs)*: Regions with $\mathcal{Y}_L > 0$ are convectively unstable.
2. *Radiative zones (RZs)*: Regions with $\mathcal{Y}_L \leq \mathcal{Y}_S < 0$ are always stable to convection. Other combinations of \mathcal{Y}_L and \mathcal{Y}_S may also be stable RZs, as detailed below in #3 and #4.
3. *“Semiconvection” zones (SZs)*: Regions with $\mathcal{Y}_S > 0$ but $\mathcal{Y}_L < 0$ are stabilized by a composition gradient despite an unstable thermal stratification. These regions can be stable RZs or linearly unstable to oscillatory double-diffusive convection (ODDC; see Garaud 2018, chapters 2 and 4).
4. *“Thermohaline” zones*: A stable thermal stratification can overcome an unstable composition gradient in regions with $\mathcal{Y}_S < \mathcal{Y}_L < 0$. These regions can be stable RZs or linearly unstable to thermohaline mixing (see Garaud 2018, Ch. 2 and 3).

In this letter, we study a three-layer 3D simulation of convection. The initial structure of the simulation is an unstable CZ (bottom, #1), a compositionally stabilized SZ (middle, #3), and a thermally stable RZ (top, #2). We examine how the boundary of the CZ evolves through entrainment. In particular, we are interested both in measuring the heights at which $\mathcal{Y}_S = 0$ and $\mathcal{Y}_L = 0$ and in determining whether those heights coincide after many convective overturn timescales.

Our simulation uses the Boussinesq approximation, which is formally valid when motions occur on length scales much smaller than the pressure scale height. This approximation fully captures nonlinear advective mixing near the CZ–SZ boundary, which is our primary focus. Our simulations use a height-dependent ∇_{rad} , and buoyancy is determined by a combination of the composition and the temperature stratification, so \mathcal{Y}_S and \mathcal{Y}_L are determined independently and self-consistently. Our simulation length scales are formally much smaller than a scale height, but a useful heuristic is to think of our 3D convection zone depth (initially one-third of the simulation domain) as being analogous to the mixing length in a 1D stellar evolution model. For details on our model setup and Dedalus (Burns et al. 2020) simulations, we refer the reader to Appendices A and B.

While μ represents the mean molecular weight in stellar modeling (e.g., Equation (2)), throughout the rest of this Letter

we will use μ to denote the composition field in our simulation. In stellar modeling, the quantity that determines convective stability (the B term in, e.g., Unno et al. 1989; Paxton et al. 2013) is obtained by accounting for the variation of pressure with composition in the full equation of state. In our simulation, we employ an ideal equation of state in which compositional stability is determined by the gradient of μ .

3. Results

In Figure 1, we visualize the composition field in our simulation near the initial state (left) and evolved state (right). Thick horizontal lines denote the convective boundaries per the Ledoux (orange, $\mathcal{Y}_L = 0$) and Schwarzschild (purple, $\mathcal{Y}_S = 0$) criteria. Initially, the bottom third of the domain is a CZ, the middle third is an SZ, and the top third is an RZ. Convection motions extend beyond $\mathcal{Y}_L = 0$ at all times; we refer to these motions as overshoot (which is discussed in Korre et al. 2019). Overshoot occurs because the Ledoux boundary is not the location where convective velocity is zero, but rather the location where buoyant acceleration changes sign due to a sign change in the entropy gradient.

The difference between the left and right panels demonstrates that the CZ consumes the SZ. Overshooting convective motions entrain low-composition material into the CZ, where it is homogenized. This process increases the size of the CZ and repeats over thousands of convective overturn times until the Ledoux and Schwarzschild criteria predict the same convective boundary. After this entrainment phase, the convective boundary stops moving. The boundary is stationary because the radiative flux renews the stable temperature gradient; there is no analogous process to reinforce the composition gradient.⁹

In Figure 2, we visualize vertical profiles in the initial state (left) and evolved state (right). Shown are the composition μ (top), the discriminants \mathcal{Y}_L and \mathcal{Y}_S (middle), and two important frequencies (bottom): the square Brunt–Väisälä frequency N^2 and the square convective frequency,

$$f_{\text{conv}}^2 = \frac{|\mathbf{u}|^2}{\ell_{\text{conv}}^2}, \quad (3)$$

with $|\mathbf{u}|$ the horizontally averaged velocity magnitude and ℓ_{conv} the depth of the Ledoux-unstable layer.

The composition is initially uniform in the CZ ($z \lesssim 1$) and RZ ($z \gtrsim 2$) but varies linearly in the SZ ($z \in [1, 2]$). We have $\mathcal{Y}_L(z \approx 1) = 0$ but $\mathcal{Y}_S(z \approx 2) = 0$. An unstable boundary layer at the base of the CZ drives the instability and has negative N^2 . For $z \gtrsim 1$, we have positive N^2 , which is larger in the RZ than in the SZ. We found similar results in simulations where N^2 was constant across the RZ and SZ.

In the evolved state (right panels), the composition (top) is well mixed in the CZ and hashed overshoot zone but decreases rapidly above the overshoot region. We take the height where the horizontally averaged kinetic energy falls below 10% of its bulk-CZ value to be the top of the overshoot zone. Rare convective events provide turbulent diffusion above the overshoot zone and smooth the profile’s transition from its CZ value to its RZ value. In this evolved state, the Schwarzschild and Ledoux criteria agree upon the location of the convective boundary (middle).

⁹ Nuclear timescales are generally much longer than dynamical timescales and can be ignored as a source of composition.

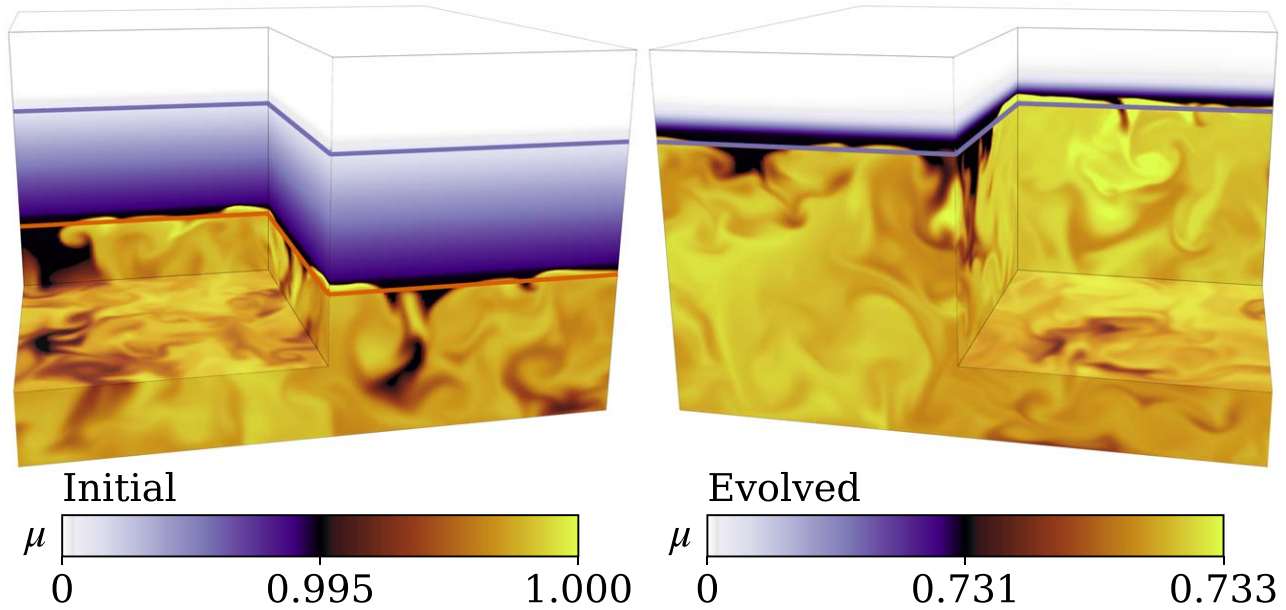


Figure 1. Volume renderings of the composition μ at early (left) and late (right) times. A stable composition gradient is denoted by the changing color from the top of the box (white) to the top of the convection zone (dark purple). The convection zone is well mixed, so we expand the color-bar scaling there; black low- μ fluid is mixed into the yellow high- μ convection zone. Orange and purple horizontal lines respectively denote the heights at which $\mathcal{Y}_L = 0$ and $\mathcal{Y}_S = 0$. The Schwarzschild and Ledoux criteria are equivalent in the right panel, so the orange line is not visible. The simulation domain spans $z \in [0, 3]$, but we only plot $z \in [0, 2.5]$ here. An animation of this figure is available online in the published article. A version is also in the supplementary materials (Anders et al. 2022b). In the animation, the initial Ledoux boundary height is denoted as a dotted orange line. The animation starts at $t = 130$ freefall time units and ends at $t = 15,520$. There are two important timescales in this problem: the short convective overturn timescale and the long entrainment timescale of the composition gradient. At early times, the movie playback speed is slow, and the evolution of convective structures can be observed over time. To show the much longer entrainment timescale, the animation speed increases by a factor of 25 for $t \in [400, 15,000]$, during which time the convective boundary advances. After $t = 15,000$, the movie returns to its original, slow playback speed and focuses again on the convective structures. The total, real-time duration of the animation is 45 s.

(An animation of this figure is available in the HTML version of this article.)

The rate at which the CZ entrains the SZ depends on the stiffness of the radiative–convective interface,

$$\mathcal{S} = \frac{N^2|_{\text{RZ}}}{f_{\text{conv}}^2|_{\text{CZ}}}, \quad (4)$$

which is related to the Richardson number $\text{Ri} = \sqrt{\mathcal{S}}$. The time to entrain the SZ is roughly $\tau_{\text{entrain}} \sim (\delta h/\ell_c)^2 R_\rho^{-1} \mathcal{S} \tau_{\text{dyn}}$ (per Fuentes & Cumming 2020, Equation (3)), where δh is the depth of the SZ, ℓ_c is the characteristic convective length scale, $R_\rho \in [0, 1]$ is the density ratio (see Garaud 2018, Equation (7)), and τ_{dyn} is the dynamical timescale, which in our simulation is the convective overturn timescale. In Figure 2, bottom-right panel, we have $f_{\text{conv}}^2|_{\text{CZ}} \approx 3 \times 10^{-3}$ and $N^2|_{\text{RZ}} \approx 10^2$, so $\mathcal{S} \approx 3 \times 10^4$. Convective boundaries in stars often have $\mathcal{S} \gtrsim 10^6$, so our simulation is in the same high- \mathcal{S} regime as stars. The value of R_ρ can vary greatly throughout the depth of an SZ in a star; we use $R_\rho = 1/10$. The relevant evolutionary timescale during the main sequence is the nuclear time τ_{nuc} . Because $\tau_{\text{nuc}}/\tau_{\text{dyn}} \gg (\delta h/\ell_c)^2 \mathcal{S}/R_\rho$ even for $\mathcal{S} \sim 10^6$, SZs should be immediately entrained by bordering CZs on the main sequence and during other evolutionary stages in which convection reaches a steady state. Note that while values of $R_\rho \ll 1$ increase τ_{entrain} , they also support efficient mixing by ODDC (see Section 4).

Finally, in Figure 3 we display a Kippenhahn-like diagram of the simulation’s evolution. This diagram demonstrates how the

CZ, SZ, and RZ boundaries evolve. The convective boundary measurements are shown as orange ($\mathcal{Y}_L = 0$) and purple ($\mathcal{Y}_S = 0$) lines. The CZ is colored orange and fills the region below the Ledoux boundary, the RZ is colored purple and fills the region above the Schwarzschild boundary, and the SZ is colored green and fills the region between these boundaries. Convective motions overshoot beyond the Ledoux boundary into a hashed overshoot zone, which we define identically to the one displayed in Figure 2. The top of the overshoot zone (black line) corresponds with the edge of the well-mixed region (Figure 2, upper right). While the Schwarzschild and Ledoux boundaries start at different heights, 3D convective mixing causes them to converge.

We briefly note that we performed additional simulations with the same initial stratification as in Figure 2 (left), but with lower values of \mathcal{S} , higher and lower values of R_ρ , and less turbulence (lower Reynolds number), and the evolutionary trends described here are present in all simulations.

4. Conclusions and Discussion

In this Letter, we present a 3D simulation of a convection zone adjacent to a compositionally stable and weakly thermally unstable region. This region is stable according to the Ledoux criterion, but unstable according to the Schwarzschild criterion. Overshooting convective motions entrain the entire Schwarzschild-unstable region until the Schwarzschild and Ledoux criteria both predict the same boundary of the convection zone.

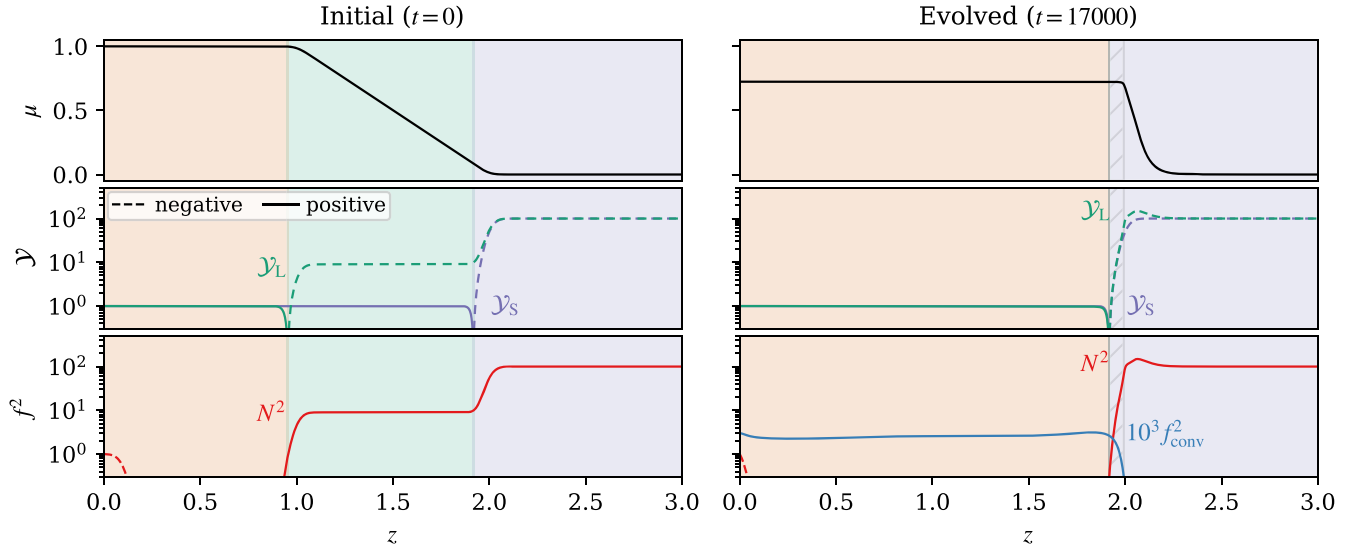


Figure 2. Horizontally averaged profiles of the composition (top), the discriminants \mathcal{Y}_S and \mathcal{Y}_L (middle, Equations (1) and (2)), and important frequencies (bottom, the Brunt–Väisälä frequency $N^2 = -\mathcal{Y}_L$ and the square convective frequency f_{conv}^2 ; see Equation (3)). Positive and negative values are respectively shown by the solid and dashed lines. We show the initial (left) and evolved (right, time-averaged over 100 convective overturn times) states. There are no motions in the initial state, so $f_{\text{conv}}^2 = 0$ and does not appear. The background color is orange in the CZ, green in the SZ, and purple in the RZ. The lightly hashed background region in the evolved RZ is the mechanical overshoot zone.

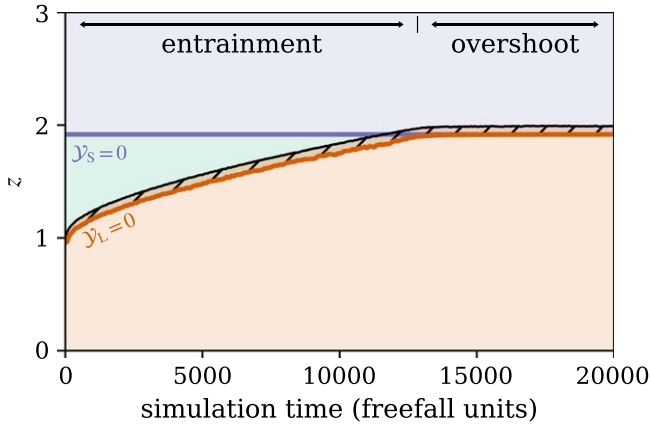


Figure 3. A Kippenhahn-like diagram of the simulation evolution. The y-axis is the simulation height, and the x-axis is the simulation time. The orange line denotes the Ledoux convective boundary ($\mathcal{Y}_L = 0$); the CZ is below this and is colored orange. The purple line denotes the Schwarzschild convective boundary ($\mathcal{Y}_S = 0$); the RZ is above this and is colored purple. The SZ between these boundaries is colored green. The black line denotes the top of the overshoot zone, which is hashed. The simulation has an “entrainment phase”, in which the CZ expands, and a pure “overshoot phase”, in which the convective boundary remains stationary.

This simulation demonstrates that the Ledoux criterion instantaneously predicts the location of the convective boundary, but the Schwarzschild criterion correctly predicts its location on evolutionary timescales (for $t_{\text{evol}} \gg (\delta h / \ell_c)^2 R_p^{-1} St_{\text{dyn}}$, see Section 3). Our 3D simulation supports the claim that logically consistent implementations of mixing length theory (Gabriel et al. 2014; Paxton et al. 2018, 2019) should have convective boundaries that are Schwarzschild stable. For example, the MESA software instrument’s “convective premixing” (CPM, Paxton et al. 2019) is consistent with our simulation. Given our results, the predictions made by 1D stellar evolution calculations should not depend on the choice of stability criterion used if/when convective boundary treatments are properly implemented and $t_{\text{evol}} \gg (\delta h / \ell_c)^2 R_p^{-1} St_{\text{dyn}}$.

In stars, SZs should often be unstable to ODDC. Mirouh et al. (2012) show that convective layers often emerge from ODDC and thus mix composition gradients more rapidly than entrainment alone; ODDC is discussed thoroughly in Garaud (2018). Moore & Garaud (2016) apply ODDC to SZs, which form outside core convection zones in main-sequence stars, and their results suggest that ODDC should rapidly mix these regions. Our simulation demonstrates that entrainment should prevent SZs from ever forming at convective boundaries.

For stages in stellar evolution where $t_{\text{evol}} \sim (\delta h / \ell_c)^2 R_p^{-1} St_{\text{dyn}}$, time-dependent convection (TDC; Kuhfuss 1986) implementations can be used to improve accuracy. These implementations should include time-dependent entrainment models to properly advance convective boundaries (e.g., Turner 1968; Fuentes & Cumming 2020).

Anders et al. (2022a) showed convective motions can extend significantly into the radiative zones of stars via “penetrative convection.” In this work, we used parameters that do not have significant penetration. This can be seen in the right panels of Figure 2 because the composition is well mixed above the convective boundary, but the thermal structure is not.

We assume that the radiative conductivity and ∇_{rad} do not depend on μ for simplicity. The nonlinear feedback between these effects should be studied in future work, but we expect that our conclusions are robust.

In summary, we find that the Ledoux criterion provides the instantaneous location of the convective boundary, and the Schwarzschild criterion provides the location of the convective boundary in a statistically stationary state; in this final state, the Ledoux and Schwarzschild criteria agree.

We thank Anne Thoul, Dominic Bowman, Jared Goldberg, Tim Cunningham, Falk Herwig, and Kyle Augustson for useful discussions, which helped improve our understanding. We thank the anonymous referee for constructive feedback, which improved the clarity of this manuscript. E.H.A. is funded as a CIERA Postdoctoral fellow and would like to thank CIERA and Northwestern University. The Flatiron Institute is supported by

the Simons Foundation. D.L. and I.G.C. are supported in part by NASA HTMS grant 80NSSC20K1280. A.E.F. acknowledges support from NSF grant Nos. AST-1814327 and AST-1908338. I.G.C. acknowledges the support of the University of Colorado George Ellery Hale Graduate Student Fellowship. M.J. acknowledges support from the Barry M. Lasker Data Science Fellowship awarded by the Space Telescope Science Institute. J.R.F. acknowledges support from a McGill Space Institute (MSI) Fellowship. This research was supported in part by the National Science Foundation under grant No. PHY-1748958, and we acknowledge the hospitality of KITP during the Probes of Transport in Stars Program. Computations were conducted with support from the NASA High End Computing (HEC) Program through the NASA Advanced Supercomputing (NAS) Division at Ames Research Center on Pleiades with allocation GID s2276.

Appendix A Model and Initial Conditions

We study incompressible Boussinesq convection in which we evolve both temperature T and concentration μ . The nondimensional equations of motion are

$$\nabla \cdot \mathbf{u} = 0 \quad (\text{A1})$$

$$\partial_t \mathbf{u} + \mathbf{u} \cdot \nabla \mathbf{u} + \nabla \varpi = \left(T - \frac{\mu}{R_\rho} \right) \hat{z} + \frac{\text{Pr}}{\text{Pe}} \nabla^2 \mathbf{u}, \quad (\text{A2})$$

$$\partial_t T + \mathbf{u} \cdot (\nabla T - \hat{z} \partial_z T_{\text{ad}}) = \nabla \cdot [\kappa_{T,0} \nabla \bar{T}] + \frac{1}{\text{Pe}} \nabla^2 T', \quad (\text{A3})$$

$$\partial_t \mu + \mathbf{u} \cdot \nabla \mu = \frac{\tau_0}{\text{Pe}} \nabla^2 \bar{\mu} + \frac{\tau}{\text{Pe}} \nabla^2 \mu', \quad (\text{A4})$$

where \mathbf{u} is velocity. Overbars denote horizontal averages and primes denote fluctuations around that average such that $T = \bar{T} + T'$. The adiabatic temperature gradient is $\partial_z T_{\text{ad}}$ and the nondimensional control parameters are

$$\begin{aligned} \text{Pe} &= \frac{u_{\text{ff}} h_{\text{conv}}}{\kappa_T}, & R_\rho &= \frac{|\alpha| \Delta T}{|\beta| \Delta \mu}, \\ \text{Pr} &= \frac{\nu}{\kappa_T}, & \tau &= \frac{\kappa_\mu}{\kappa_T}, \end{aligned} \quad (\text{A5})$$

where the nondimensional freefall velocity is $u_{\text{ff}} = \sqrt{|\alpha| g h_{\text{conv}} \Delta T}$ (with gravitational acceleration g), h_{conv} is the initial depth of the convection zone, the constant $\Delta \mu$ is the initial composition change across the Ledoux-stable region, the constant $\Delta T = h_{\text{conv}} (\partial_z T_{\text{rad}} - \partial_z T_{\text{ad}})$ is the initial superadiabatic temperature scale of the convection zone, $\alpha \equiv (\partial \ln \rho / \partial T)|_\mu$ and $\beta \equiv (\partial \ln \rho / \partial \mu)|_T$ are, respectively, the coefficients of expansion for T and μ , the viscosity is ν , κ_T is the thermal diffusivity, and κ_μ is the compositional diffusivity. In stellar structure modeling, $R_\rho = |N_{\text{structure}}^2 / N_{\text{composition}}^2|$ is the ratio of respectively the thermal and compositional components of the Brunt–Väisälä frequency as measured in a semiconvection zone or thermohaline zone. Equations (A1)–(A4) are identical to Equations (2)–(5) in Garaud (2018), except we modify the diffusion coefficients acting on \bar{T} ($\kappa_{T,0}$) and $\bar{\mu}$ (τ_0). By doing this, we keep the turbulence (Pe) uniform throughout the domain while also allowing the radiative temperature gradient $\partial_z T_{\text{rad}} = -\text{Flux} / \kappa_{T,0}$ to vary with height. We

furthermore reduce diffusion on $\bar{\mu}$ to ensure its evolution is due to advection.

We define the Ledoux and Schwarzschild discriminants

$$\mathcal{Y}_S = \left(\frac{\partial T}{\partial z} \right)_{\text{rad}} - \left(\frac{\partial T}{\partial z} \right)_{\text{ad}}, \quad \mathcal{Y}_L = \mathcal{Y}_S - R_\rho^{-1} \frac{\partial \mu}{\partial z}, \quad (\text{A6})$$

and in this nondimensional system, the square Brunt–Väisälä frequency is $N^2 = -\mathcal{Y}_L$.

We study a three-layer model with $z \in [0, 3]$,

$$\left(\frac{\partial T}{\partial z} \right)_{\text{rad}} = \left(\frac{\partial T}{\partial z} \right)_{\text{ad}} + \begin{cases} -1 & z \leq 2 \\ 10R_\rho^{-1} & z > 2 \end{cases}, \quad (\text{A7})$$

$$\frac{\partial \mu_0}{\partial z} = \begin{cases} 0 & z \leq 1 \\ -1 & 1 < z \leq 2, \\ 0 & 2 > z \end{cases}, \quad (\text{A8})$$

We set $(\partial T / \partial z)_{\text{ad}} = -1 - 10R_\rho^{-1}$. The initial temperature profile has $\partial_z T_0 = \partial_z T_{\text{rad}}$ everywhere except between $z = [0.1, 1]$ where $\partial_z T_0 = \partial_z T_{\text{ad}}$. Step functions are not well represented in pseudospectral codes, so we use smooth Heaviside functions (Equation (B1)) to construct these piecewise functions. To obtain T_0 , we numerically integrate the smooth $\partial_z T_0$ profile with $T_0(z=3) = 1$. To obtain μ_0 , we numerically integrate the smooth Equation (A8) with $\mu_0(z=0) = 0$.

For boundary conditions, we hold $\partial_z T = \partial_z T_0$ at $z=0$, $T = T_0$ at $z=3$, and we set $\partial_z \mu = \hat{z} \cdot \mathbf{u} = \hat{x} \cdot \partial_z \mathbf{u} = \hat{y} \cdot \partial_z \mathbf{u} = 0$ at $z = [0, 3]$. The simulation in this work uses $\text{Pe} = 3.2 \times 10^3$, $R_\rho^{-1} = 10$, $\text{Pr} = \tau = 0.5$, $\tau_0 = 1.5 \times 10^{-3}$, and $\kappa_{T,0} = \text{Pe}^{-1} [(\partial T / \partial z)_{\text{rad}}|_{z=0}] / (\partial T / \partial z)_{\text{rad}}$. The convective cores of main-sequence stars with $2M_\odot \lesssim M_* \lesssim 10M_\odot$ have $\text{Pe} = \mathcal{O}(10^6)$, $\tau \approx \text{Pr} = \mathcal{O}(10^{-6})$, and a stiffness of $\mathcal{S} = \mathcal{O}(10^{6-7})$ (see Jermyn et al. 2022, ‘‘An Atlas of Convection in Main-Sequence Stars,’’2022, in preparation). Our simulation is as turbulent as possible while also achieving the long-term entrainment of the Ledoux boundary and is qualitatively in the same regime as stars ($\text{Pe} \gg 1$, $\text{Pr} < 1$, $\mathcal{S} \gg 1$). Unfortunately, stars are both more turbulent and have stiffer boundaries than can be simulated with current computational resources.

Appendix B Simulation Details and Data Availability

We time-evolve Equations (A1)–(A4) using the Dedalus pseudospectral solver (Burns et al. 2020, git commit 1339061) using time-stepper SBDF2 (Wang & Ruuth 2008) and CFL safety factor 0.3. All variables are represented using a Chebyshev series with 512 terms for $z \in [0, 2.25]$, another Chebyshev series with 64 terms for $z \in [2.25, 3]$, and Fourier series in the periodic x and y directions with 192 terms each. Our domain spans $x \in [0, L_x]$, $y \in [0, L_y]$, and $z \in [0, L_z]$ with $L_x = L_y = 4$ and $L_z = 3$. To avoid aliasing errors, we use the 3/2 dealiasing rule in all directions. To start our simulations, we add random noise temperature perturbations with a magnitude of 10^{-6} to the initial temperature field.



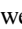


Spectral methods with finite coefficient expansions cannot capture true discontinuities. To approximate discontinuous functions such as Equations (A7) & (A8), we define a smooth Heaviside step function centered at $z = z_0$,

$$H(z; z_0, d_w) = \frac{1}{2} \left(1 + \text{erf} \left[\frac{z - z_0}{d_w} \right] \right). \quad (\text{B1})$$

where erf is the error function, and we set $d_w = 0.05$.

We produced Figures 2 and 3 using matplotlib (Hunter 2007; Caswell et al. 2021). We produced Figure 1 using plotly (Plotly Technologies Inc. 2015) and matplotlib. The Python scripts used to run the simulation and to create the figures in this paper are publicly available in a git repository (https://github.com/evanhanders/schwarzschild_or_ledoux); the data in the figures is available online in a Zenodo repository (Anders et al. 2022b).

ORCID iDs

Evan H. Anders  <https://orcid.org/0000-0002-3433-4733>
 Adam S. Jermyn  <https://orcid.org/0000-0001-5048-9973>
 Daniel Lecoanet  <https://orcid.org/0000-0002-7635-9728>
 Adrian E. Fraser  <https://orcid.org/0000-0003-4323-2082>
 Imogen G. Cresswell  <https://orcid.org/0000-0002-4538-7320>
 Meridith Joyce  <https://orcid.org/0000-0002-8717-127X>
 J. R. Fuentes  <https://orcid.org/0000-0003-2124-9764>

References

- Anders, E. H., Jermyn, A. S., Lecoanet, D., & Brown, B. P. 2022a, *ApJ*, **926**, 169
- Anders, E. H., Jermyn, A. S., Lecoanet, D., et al. 2022b, Supplemental Materials for “Schwarzschild and Ledoux are Equivalent on Evolutionary Timescales”, 1.1, Zenodo, doi:10.5281/zenodo.6344868
- Andrassy, R., Herwig, F., Woodward, P., & Ritter, C. 2020, *MNRAS*, **491**, 972
- Andrassy, R., Higl, J., Mao, H., et al. 2021, arXiv:2111.01165
- Basu, S. 2016, *LRSP*, **13**, 2
- Basu, S., Verner, G. A., Chaplin, W. J., & Elsworth, Y. 2012, *ApJ*, **746**, 76
- Burns, K. J., Vasil, G. M., Oishi, J. S., Lecoanet, D., & Brown, B. P. 2020, *PhRvR*, **2**, 023068
- Carlos, M., Meléndez, J., Spina, L., et al. 2019, *MNRAS*, **485**, 4052
- Caswell, T. A., Droettboom, M., Lee, A., et al. 2021, matplotlib/matplotlib: REL: v3.3.4, v3.3.4, 4 Zenodo, doi:10.5281/zenodo.4475376
- Claret, A., & Torres, G. 2018, *ApJ*, **859**, 100
- Cristini, A., Hirschi, R., Meakin, C., et al. 2019, *MNRAS*, **484**, 4645
- Dumont, T., Palacios, A., Charbonnel, C., et al. 2021, *A&A*, **646**, A48
- Farmer, R., Renzo, M., de Mink, S. E., Marchant, P., & Justham, S. 2019, *ApJ*, **887**, 53
- Fuentes, J. R., & Cumming, A. 2020, *PhRvF*, **5**, 124501
- Gabriel, M., Noels, A., Montalbán, J., & Miglio, A. 2014, *A&A*, **569**, A63
- Garaud, P. 2018, *AnRFM*, **50**, 275
- Georgy, C., Saio, H., & Meynet, G. 2021, *A&A*, **650**, A128
- Hunter, J. D. 2007, *CSE*, **9**, 90
- Johnston, C. 2021, *A&A*, **655**, A29
- Jones, S., Andrassy, R., Sandalski, S., et al. 2017, *MNRAS*, **465**, 2991
- Joyce, M., & Chaboyer, B. 2018, *ApJ*, **864**, 99
- Kaiser, E. A., Hirschi, R., Arnett, W. D., et al. 2020, *MNRAS*, **496**, 1967
- Korre, L., Garaud, P., & Brummell, N. H. 2019, *MNRAS*, **484**, 1220
- Kuhfuss, R. 1986, *A&A*, **160**, 116
- Meakin, C. A., & Arnett, D. 2007, *ApJ*, **667**, 448
- Mehta, A. K., Buonanno, A., Gair, J., et al. 2022, *ApJ*, **924**, 39
- Mirouh, G. M., Garaud, P., Stellmach, S., Traxler, A. L., & Wood, T. S. 2012, *ApJ*, **750**, 61
- Moore, K., & Garaud, P. 2016, *ApJ*, **817**, 54
- Morrell, S. A. F. 2020, PhD thesis, University of Exeter
- Paxton, B., Cantiello, M., Arras, P., et al. 2013, *ApJS*, **208**, 4
- Paxton, B., Schwab, J., Bauer, E. B., et al. 2018, *ApJS*, **234**, 34
- Paxton, B., Smolec, R., Schwab, J., et al. 2019, *ApJS*, **243**, 10
- Pedersen, M. G., Aerts, C., Pápics, P. I., et al. 2021, *NatAs*, **5**, 715
- Pinsonneault, M. 1997, *ARA&A*, **35**, 557
- Plotly Technologies Inc. 2015, Collaborative data science, Montreal, QC: Plotly Technologies Inc., <https://plot.ly>
- Salaris, M., & Cassisi, S. 2017, *RSOS*, **4**, 170192
- Scott, L. J. A., Hirschi, R., Georgy, C., et al. 2021, *MNRAS*, **503**, 4208
- Sestito, P., & Randich, S. 2005, *A&A*, **442**, 615
- Silva Aguirre, V., Ballot, J., Serenelli, A. M., & Weiss, A. 2011, *A&A*, **529**, A63
- Staritsin, E. I. 2013, *ARep*, **57**, 380
- Turner, J. S. 1968, *JFM*, **33**, 183
- Unno, W., Osaki, Y., Ando, H., Saio, H., & Shibahashi, H. 1989, Nonradial Oscillations of Stars (Tokyo: Univ. of Tokyo Press)
- Viani, L. S., & Basu, S. 2020, *ApJ*, **904**, 22
- Wang, D., & Ruuth, S. J. 2008, *JCM*, **26**, 838
- Woodward, P. R., Herwig, F., & Lin, P.-H. 2015, *ApJ*, **798**, 49